F. P. Vidal, J. M. Létang, G. Peix et P. Clœtens: Investigation of artefact sources in synchrotron microtomography via virtual X-ray imaging. *Nuclear Instruments and Methods in Physics Research B* (June 2005), Elsevier. Volume 234, Issue 3, pp. 333-348.

DOI: 10.1016/j.nimb.2005.02.003

Keywords: X-ray microtomography; Artefact; Deterministic simulation (ray-tracing); Monte Carlo method; Phase contrast; Modulation transfer function.

PACS: 87.59.F; 07.85.Q; 07.05.T; 02.50.N; 42.15.D

```
@ARTICLE{Vidal2005NuclInstrumMethB,
  author = {F. P. Vidal and J. M. L\'etang and G. Peix and P. Cl{\oe}tens},
  title = {Investigation of artefact sources in synchrotron microtomography
via virtual X-ray imaging},
  journal = {Nuclear Instruments and Methods in Physics Research B},
  year = {2005},
  volume = {234},
  pages = {333-348},
  number = {3},
  month = Jun,
  abstract = {Qualitative and quantitative use of volumes reconstructed by computed-tomography (C
  doi = {10.1016/j.nimb.2005.02.003},
  keywords = {X-ray microtomography; Artefact; Deterministic simulation (ray-tracing);
Monte Carlo method; Phase contrast; Modulation transfer function},
  publisher = {Elsevier}
}
```

Investigation of artefact sources in synchrotron microtomography via virtual X-ray imaging

Franck P. Vidal [1], Jean Michel Létang [1], Gilles Peix [1], and Peter Cloetens [2]
[1] CNDRI (Laboratory of Nondestructive Testing using Ionizing Radiations),
INSA-Lyon Scientific & Technical University, 69621 Villeurbanne cedex, France
[2] European Synchrotron Radiation Facility, BP 220, 38043 Grenoble, France

Abstract

Qualitative and quantitative use of volumes reconstructed by computed-tomography (CT) can be compromised due to artefacts which corrupt the data. This article illustrates a method based on virtual X-ray imaging to investigate sources of artefacts which occur in microtomography using synchrotron radiation. In this phenomenological study, different computer simulation methods based on physical X-ray properties, eventually coupled with experimental data, are used in order to compare artefacts obtained theoretically to those present in a volume acquired experimentally, or to predict them for a particular experimental setup. The article begins with the presentation of a synchrotron microtomographic slice of a reinforced fibre composite acquired at the European Synchrotron Radiation Facility (ESRF) containing streak artefacts. This experimental context is used as the motive throughout the paper to illustrate the investigation of some artefact sources. First, the contribution of direct radiation is compared to the contribution of secondary radiations. Then, the effect of some methodological aspects are detailed, including under-sampling, sample and camera misalignment, sample extending outside of the field of view, and photonic noise. The effect of harmonic components present in the experimental spectrum are also simulated. Afterwards, detector properties, such as its impulse response or defective pixels, are taken into account. Finally, the importance of phase contrast effects is evaluated. In the last section, this investigation is discussed by putting emphasis on the experimental context which is used throughout this paper.

Keywords: X-ray microtomography; Artefact; Deterministic simulation (ray-tracing); Monte Carlo method; Phase contrast; Modulation transfer function.

PACS: 87.59.F; 07.85.Q; 07.05.T; 02.50.N; 42.15.D.

1 Introduction

Computed tomography (CT) [31, 38], a technique developed by Hounsfield in 1972 [27], has become a common investigation tool to study the internal structure of materials [50, 37]. CT is a multi-angular acquisition followed by a numerical reconstruction procedure which yields, from a sufficient number of projections, a three-dimensional (3D) dataset consisting of trans-axial planes of X-ray attenuation coefficients through the sample. However, the acquisition and the reconstruction processes can generate spurious images due to artefacts, which might prevent a quantitative use of such data. The basic sources of artefacts have been studied in detail in the literature [31, 28]. Let us recall the main ones. First of all, due to the necessary discrete mathematical approach of the problem, under-sampling the number of projections or under-sampling the number of pixels of the detector results in aliasing. When a polychromatic beam is considered, strong artefacts, usually called "cupping effect", appear due to beam hardening [10]. If there are defective or badly corrected

pixels in the projection, ring artefacts occur in the reconstructed data [46]. Lack of uniformity in the output of X-ray tubes, detector sensitivity, changes in voltage supply, incomplete field of view [39], and scattering were reported to generate artefacts [47]. Nevertheless most studies regarding artefacts in tomography have been conducted only in the medical field. Some of them are specific to this scope, like streaks due to metallic implants, boundary splitting and subtle distortions of shape due to patient movement [54], or artefacts caused by aortic motion [43] and respiration [24]. The influence of data acquisition parameters (collimation, pitch and angle of inclination) on artefacts in reconstructed images has specifically been challenged in the case of colonography [51]. On some reconstructed images, dark and bright fringes located at density edges can be observed due to phase contrast phenomena [11].

Nowadays, computers are fast enough to enable the simulation of the whole X-ray imaging chain, from the source to the detector. Simulation tools and models are numerous. They allow scientists to simulate experiments, to optimise their parameters [36], to assist experts in their analytical approach of radiography [6], as well as to register 3D to 2D imaging systems [49, 40]. There are basically two different kinds of X-ray simulation algorithms in use:

- probabilistic method, based on Monte Carlo trials,
- determinist or analytic method, based on ray-tracing.

Simulation by Monte Carlo [1, 44, 6] consists of the individual tracking of each particle (*e.g.* photon or electron in the case of X-ray simulation). Such algorithms are able to follow step-by-step each particle during its different interactions with matter. At each step of the simulation, several interactions are possible for each particle. These events are randomly chosen, their probability respecting physical laws. Ray-tracing is a determinist algorithm, originally designed for image synthesis in the visible domain [22, 48]. In the 3D space, a straight line from the observer (viewpoint) to a pixel of a projection plane is called a ray. For each pixel, intersections between a ray and 3D objects must be computed. Only the closest intersection to the observer is relevant in the visible light case, indeed others are hidden if there is no transparency. The ray-tracing principle has been adapted to X-ray simulation [20, 23]. In this case, every intersection has to be considered. This allows the computation of radiation attenuation, considering the thickness crossed by a ray into objects characterised by their material properties. The two kinds of algorithm are not exclusive, but complementary:

- The Monte Carlo approach is slow. Several days can be needed to get an image with an acceptable noise level (*e.g.* 1%), but it incorporates each kind of photon/matter interaction into account (scattering, fluorescence, electron processes).
- The second approach is fast and does not produce any noise. To simulate realistic images, Poisson noise in each photon energy channel can be added afterward. A full sinogram can be simulated from CAD models in a few minutes using a current computer. However it is only suited to directly transmitted photons.

The purpose of this paper is to investigate a method based on X-ray simulation to study the influence of the different sources of artefacts in a given microtomographic setup. Although work investigating various causes of artefacts has been done, a generic method to diagnose the origin of artefacts observed in a given reconstructed volume needs to be conducted. This topic may be of importance for physicians to optimise the data acquisition process, by providing them with acquisition procedures to avoid or reduce artefacts depending on the material nature of a particular studied sample. To illustrate the proposed method, a specific microtomographic volume acquired by synchrotron radiations [37] is used throughout the paper. In this particular reconstructed composite material, dark streak artefacts are present, preventing the quantitative use of the 3D data.

In Section 2, we begin with an overview of two similar tomographic acquisitions, carried out at ESRF, of Ti/SiC fibre composites. In one sample, the fibre's core is made of carbon while in the second it is made of tungsten. While the reconstruction of the sample with carbon cores

seems to be free of artefacts, the reconstruction of the sample with tungsten cores generates spurious streaks. Section 3.1 evaluates the importance of each photon/matter interaction and their respective degradation of the X-ray image. The influence of methodological parameters which have to be taken into account for any acquisition, such as under-sampling, sample and camera misalignment, objects extending outside the scan field of view and photonic noise, are reviewed in Sections 3.2 to 3.5. The role of harmonic components possibly present in the incident beam is reported in Section 3.6. In Section 3.7, a method to estimate the impulse response of an X-ray camera is presented and applied to the FReLoN (Fast Read-out Low Noise) camera based detector used at the ID19 beamline [34]. Then the corresponding effects are simulated. Degradations due to defective or badly corrected pixels of the detector are presented is Section 3.8. Finally, phase contrast artefacts are evaluated in Section 3.9.

2 Background

Given an ideal detector and a monochromatic X-ray source, a volume reconstructed by tomography is a map of linear attenuation coefficients for that particular energy. However, in practice several artefacts may occur in reconstructed volumes.

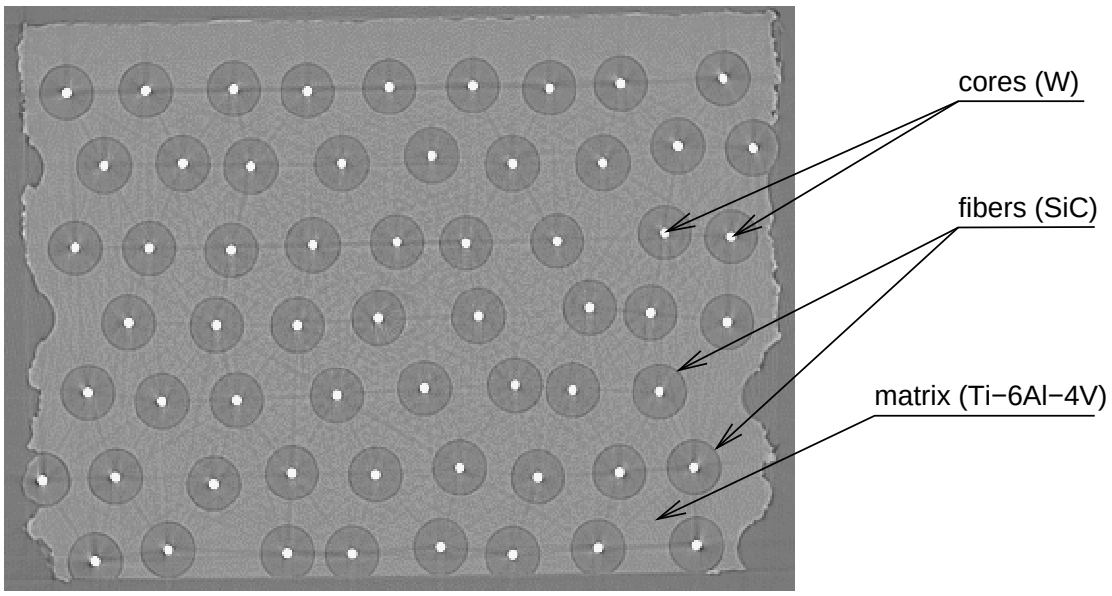

Figure 1: Slice reconstructed by microtomography, containing artefacts. Experiment carried out at ESRF on the ID19 beamline (distance source/detector: 145 m (parallel beam)). Distance detector/sample, 80 mm. Detector: 0.5 mm thick substrate supporting a YAG:Ce fluorescent layer deposited. CCD camera: 1024 × 1024 pixels resolution. Effective pixel size: 1.9 µm. Synchrotron radiation: 33 keV (500 eV FWHM) in energy selected with a Ru/B_4C multilayer. 900 projections (almost half of optimal). Angular span: 180°.

As an example, Figure 1 shows a typical reconstructed slice of an Ti/SiC fibre composite acquired at ESRF. The reconstruction algorithm is the standard filtered backprojection [31] with a cut-off frequency half the sampling [41]. The matrix is a mixture composed of titanium (90%), aluminium (6%) and vanadium (4%). Fibres are silicon carbide and their cores (the bright spots in Figure 1) are tungsten. Two kinds of artefacts are clearly visible in Figure 2, showing real and theoretical intensity profiles, and in Figure 3, an enlarged region of interest (ROI) of the initial slice:

1. black and white fringes at the silicon carbide edges; these phase artefacts are similar to some image enhancement techniques like unsharp masking [29] with a Laplacian filter [14];

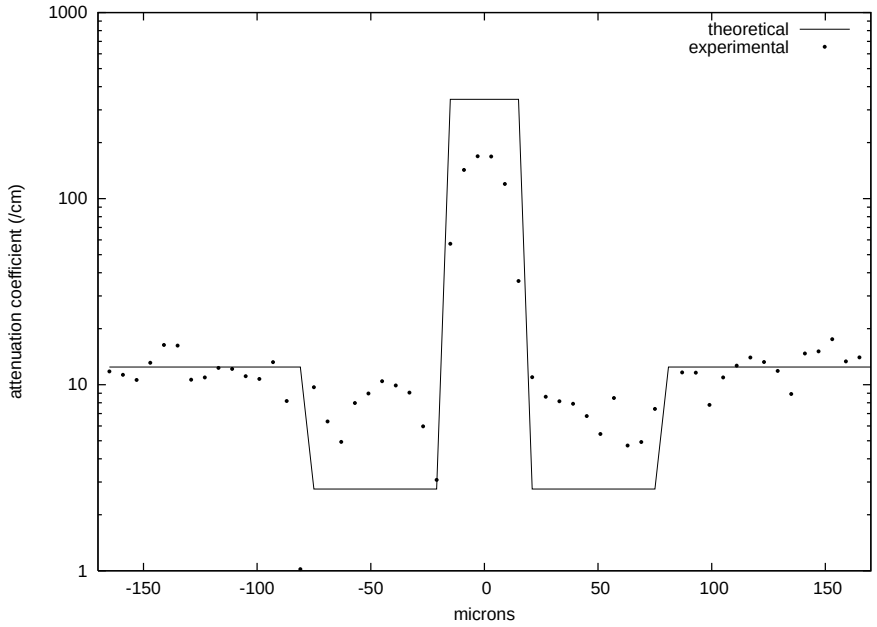

Figure 2: Comparison between an experimental intensity profile (extracted from Figure 1) and the corresponding theoretical values. The profile is radially sampled across a fibre. The reconstructed voxel size is 6 microns.

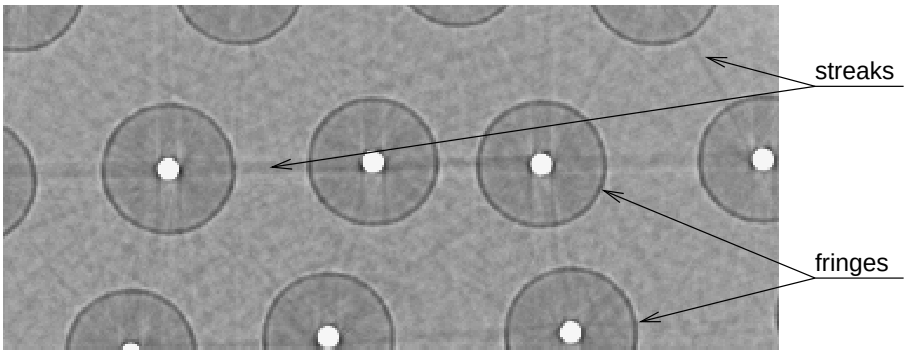

Figure 3: Extract of Figure 1. The fibre diameter is 140 microns and its core diameter is 30 microns.

Material	Linear attenuation coefficient (μ in cm^{-1})	
	theoretical	experimental
SiC	2.750	6.7 ($\sigma = 4.2$)
Ti-6Al-4V	12.449	14.6 ($\sigma = 3.3$)
W	341.61	172.3 ($\sigma = 7.9$)

Table 1: Comparison of theoretical and experimental linear attenuation coefficients at 33 keV. Experimental values (mean and standard deviation) are computed from intensity histograms for each material, manually segmented in the image via a binary mask.

2. dark streaks with bright borders, located along alignments of high density tungsten cores.

As these streaks are darker, linear attenuation coefficients are underestimated in the artefacts area. Comparing the attenuation coefficients in this slice to the corresponding theoretical values [4, 5], it is found that computed coefficients are wrong, particularly at artefact and tungsten core regions (Table 1). Most notably, the tungsten value is underestimated by a factor of 2. On the other hand, Figure 4 is the result of a tomographic reconstruction where the cores are carbon, which has very low absorption compared to tungsten. Dark and bright fringes around the fibre cores are still clearly visible, but there are no longer any dark streaks.

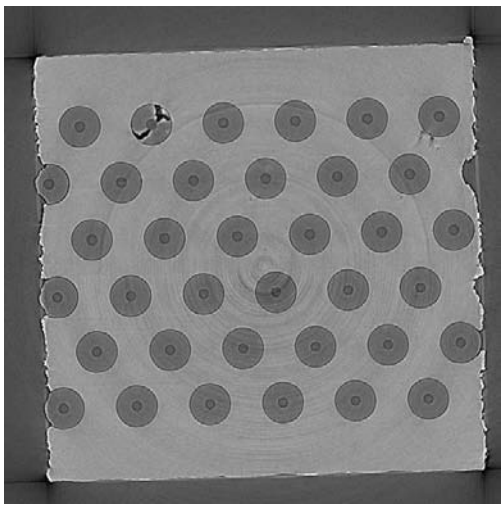

Figure 4: Slice of a titanium composite reinforced with SiC fibres with carbon core reconstructed by tomography. Experiment carried out at ESRF on ID19 beamline. Distance detector/sample: 60 mm. Pixels size: 1.4 µm. Synchrotron radiation: 30 keV (450 eV FWHM) in energy. 1200 projections. Angular span: 180°.

In this study, we apply our virtual imaging approach to those titanium composites with SiC fibres containing tungsten or carbon cores. The goal is to evaluate and understand all relevant possible causes of artefacts, using both real experiments and simulation tools.

3 Investigation of artefacts origins

In order to diagnose the different causes which might have generated artefacts in a given 3D image, we investigate in this section all relevant origins of artefacts which could occur in synchrotron microtomography, using simulations of X-ray imaging and experimental data complementarily.

3.1 Interactions

This subsection evaluates the relative importance of the directly transmitted radiation with respect to other radiations (scattering, fluorescence, *etc.*) that could be expected in a titanium composite with tungsten core fibres. As stated previously, simulations by the Monte Carlo method are able to follow each photon during its different interactions with matter. The aim of such a simulation is twofold. First, in order to use a fast ray-tracing algorithm which ignores scattering, it is fundamental to ascertain that scattering is negligible compared to directly transmitted photons. Second, we have to determine whether a particular kind of interaction is important enough to generate artefacts in the case of the considered sample.

Basically at low X-ray energies, three main kinds of interaction between photons and matter are likely to degrade X-ray images:

- Rayleigh scattering;
- Compton scattering;
- Fluorescence photon emission.

To carry out probabilistic simulations, GEANT4 (for GEometry ANd Tracking), a library developed by CERN (European Organisation for Nuclear Research) is used to simulate the passage of particles through matter [1]. A simulation was performed using a 3D scene composed of a monochromatic parallel X-ray beam at 33 keV, similar to the real experiment, an Ti/SiC fibre composite simulation phantom and a detector. As far as the ratio direct *vs* other radiations is concerned, the worst case occurs when considering pixels located along alignments of tungsten cores. When a simulation of 4 aligned fibres is carried out, 99.89% of the energy received by the detector behind the cores corresponds to directly transmitted photons. Table 2 summarises the repartition of the remaining 0.11% of the received energy. This simulation shows that, for this composite material, scattering, fluorescence and Bremsstrahlung photons are negligible with respect to directly transmitted photons. The result is twofold:

1. those radiations can be inactivated in further simulations; consequently, simulations can be performed in this example case by ray-tracing using virtual X-ray imaging, a faster technique, which enables tomographic acquisition simulations in an acceptable computation time [20, 21];
2. artefacts cannot be present in the reconstructed volume on account of non direct radiations.

Radiation	Percentage in energy received
Rayleigh scattering	90.66%
Compton scattering	4.93%
Scattering photons (order ≥ 2)	3.29%
Fluorescence & Bremsstrahlung photons	1.12%

Table 2: Decomposition of the energy received by the detector behind 4 aligned tungsten cores other than direct radiation, i.e. 0.11% of the total energy.

Note that according to Tofts and Gore [47], the amount of scattering radiations has to be reduced or corrected down to 1% of the incident beam energy in CT scanners. Also note that, for the same energy absorbed by the detector coming from non direct radiations, the artefacts magnitude is highly dependent on the relative importance of the different interaction types. For example, Rayleigh photons give rise to fewer artefacts than Compton ones, because of the Rayleigh peaked probability in the incident direction. Nevertheless, it is still possible to deal with non directly transmitted radiations in three ways:

- by using a specific mechanical device, such as a collimation grid, in order to get rid of photons which are not parallel to the incident x-ray beam, but this is quite difficult at the resolution of the experiment (1.9 µm);
- by tuning the incident X-ray spectra to change of interaction domain; for example, reducing the incident energy will increase the photoelectric absorption with respect to the scattering;
- by image processing or inverse problem techniques; the quantitative data can, for example, be recovered by physical model based restoration [18]. Virtual X-ray imaging could in this case advantageously be used to reduce those artefacts via some iterative optimisation reconstruction scheme.

3.2 Aliasing

Like any technique dealing with sampled signals, errors can occur in CT images due to insufficiency of data caused by undersampling when the continuous signal is converted into a discrete form. In tomography, lack of data produces artefacts usually called aliasing distortions. Two sampling parameters are identified, the detector pixel number and the number of recorded projections. Nyquist observed that a signal must be sampled at least twice during each cycle of the highest frequency of the signal. Let us consider N_{ray}, the number of pixels of the detector, and P_{proj} the number of projections uniformly distributed over 180°. If projection data are under-sampled, or if not enough projections are recorded, then there will be insufficiency of data. Nevertheless, a pixel binning can be used to reduce the size of the projection. According to [31], the Nyquist theorem is satisfied when the number of projections is:

$$P_{\text{proj}} = \frac{\pi}{2} \times N_{\text{ray}} \tag{1}$$

Aliasing artefacts [31] generally consist of streaks, Gibbs phenomenon, and Moire patterns (the reconstruction algorithm being inherently not perfect), and may translate to spurious images if Equation (1) is not adequately satisfied. In such a case, decreasing the number of samples in each projection, or increasing the number of projections, reduces aliasing artefacts to some extent. Nevertheless, to check the effect of aliasing, different tomographic scans were simulated with different amounts of projections and keeping the number of pixels constant. According to Equation (1), at least 1609 projections were required for a 180° angular span if there were 1024 pixels per projection. The Ram-Lak apodising function with a bandwidth of 0.5 was used [41]. Images in Figure 5 show the effects of both under and oversampling.

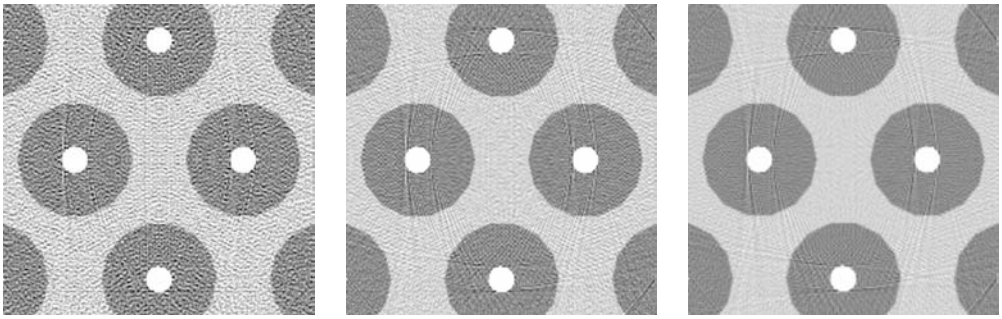

(a) (b) (c)

Figure 5: Three extracts of tomographic scans simulated using a 33 keV monochromatic beam, a 1024 pixel detector, and different numbers of projections uniformly distributed over 180°. (a) 450 projections, (b) 900 projections, and (c) 1609 projections.

In the present case, undersampling decreases the visual quality of reconstructed slice by adding a noise pattern to the image (Figure 5(a)). On the other hand, oversampling enhances only slightly the visual quality of the reconstructed image. Indeed, since there are sharp edges (*i.e.* attenuation steps) in the sample, aliasing must occur whatever the sampling frequency is, because the support of the Fourier spectrum of a step function is infinity.

3.3 Sample and camera misalignment

The reconstruction process requires the geometry of the whole tomographic setup to be precisely determined, notably the relative location and orientation of the camera, source and sample. In tomography for nondestructive testing, it is more usual to rotate the sample rather than the coupled detector/X-ray source. Consequently, it is easier to design a system which fulfils the necessary conditions: camera centred and perpendicular to the X-ray beam, rotation axis parallel to the camera and vertical. However, some tomographic systems are more subject to misalignments,

e.g. open systems like C-arms in medical applications [25]: the geometry changes during the angular scan, and the calibration parameters may drift over time. A sound calibration scheme must therefore be set. The tomographic setup is usually pre-calibrated during an off-line stage [33], but some parameters are also determined during or after the scan, *e.g.* the location of the rotation axis in the detector plane is often computed via a correlation process between two projections 180 degrees apart. Reasons for inaccuracy or misalignment are several:

1. the location of the axis of rotation is badly determined (*e.g.* the software failed to compute its location),
2. the geometrical parameters have drifted,
3. the physical position in the testing device moves during the scan,
4. the sample is a dynamic process (compression, flow...)

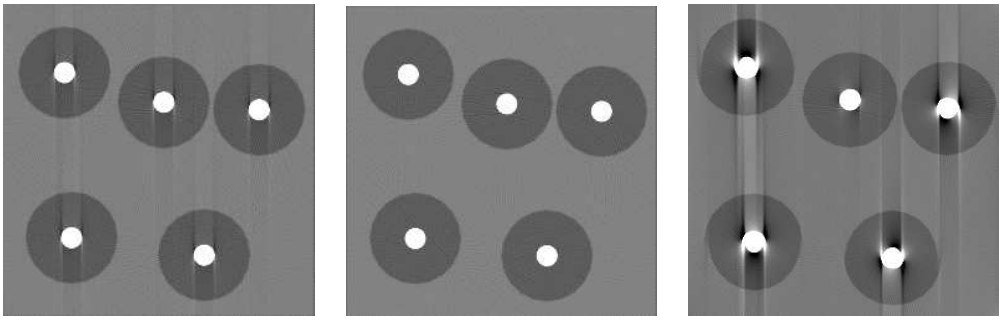

(a) (b) (c)

Figure 6: Simulated tomographic scan reconstructed using an inaccurately calibrated tomographic setup. Acquisition parameters are similar to Figure 1 unless mentioned. (a) Axis of rotation is shifted by 2 pixels, (b) the camera is misaligned by 1 degree, (c) same as (b) but the distance source/detector is 10 mm.

Figure 6 illustrates the effect of a misaligned acquisition setup. In Figure 6(a) the location of the axis of rotation used during the reconstruction process is shifted by 2 pixels with respect to the true one. In Figures 6(b) and (c) the detector plane is rotated by 1 degree around its diagonal for two different source/detector distances. Spurious shapes (half-moon like) typically appear in the reconstructed volume along sharp attenuation drops. However the characteristics of the resulting distortions greatly depends on the overall geometry. A misaligned camera simply translates to a slight anamorphose for a parallel beam in Figure 6(b), but the same misalignment in Figure 6(c) gives rise to strong artefacts when the camera solid angle from the source is bigger (cone half angle of 7.8 degrees). It must be noted that at ESRF the source is located very far from the sample (145 m at ID19), and the effect of a slight misalignment will not be detected.

There are various ways to reduce these misalignment artefacts. The rotation stage can be redesigned, and/or a new calibration procedure be set. But in the general case, especially when a dynamic process is imaged, a complete motion compensation/estimation procedure has to be developed [7]. Virtual X-ray imaging could in such a framework refine the overall 3D geometry during the reconstruction stage.

3.4 Limited field of view

In most tomographic acquisition setups, the projection of the whole sample generally remains completely included into the detector field of view during the angular scan. But the sample dimensions might sometimes be larger than the detector, then some parts of the projection of the sample can extend outside the field of view. Tofts [47] showed that artefacts due to such

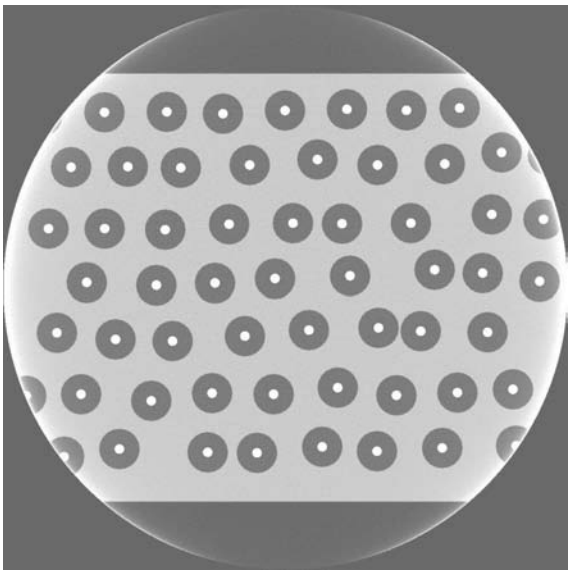

Figure 7: Tomographic scan simulated using a sinogram cropped by a third of its full size (acquisition parameters similar to Figure 1).

missing data result in an "arctan"-like global perturbation of the attenuation coefficients in the reconstructed image, more specifically along the peripheral areas where the sample extends outside of the field of view.

To simulate a sample which extends outside of the detector field of view, the sinogram was cropped with zero padding: in each projection, a third of the image data in the direction of the rotation plane is dismissed. A typical reconstruction is shown in Figure 7. The left and right sides of the reconstructed disk, where the sample extends outward, are brighter. On these specific areas, attenuation information is present in some projections and missing in other projections. Consequently, these particular parts are considered more attenuating than they really are. To cope with those truncation artefacts, a multiresolution approach can be used [8], or projections may be extended [52].

3.5 Noise

Photons are more heavily attenuated by materials with high effective atomic number, especially when the incident energy is weak. When such highly attenuating structures are aligned, the number of detected photons in those regions of the camera is very low. As a consequence, the attenuation is over-estimated along these alignments if the number of detected photons is close to zero: bright streaks appear as Figure 8 clearly shows.

To avoid this kind of artefact due to poor counting statistics, the integration time of the flat-field should be set to fill the entire dynamic range of the detector. However, when the sample is imaged, some areas of the detector still do not receive a sufficient number of photons, so an image integration process must be used or the X-ray energy should be increased. Nevertheless, for a given noise level, data collection is likely to be much faster in tomography by synchrotron radiation, compared to tomography with classic or micro-focus X-ray tubes. Indeed, the photon flux in the case of synchrotron radiation is usually very important, even when monochromators are used. However, these artefacts due to the presence of highly attenuating structures cannot sometimes be reduced to acceptable levels without some prior knowledge [53].

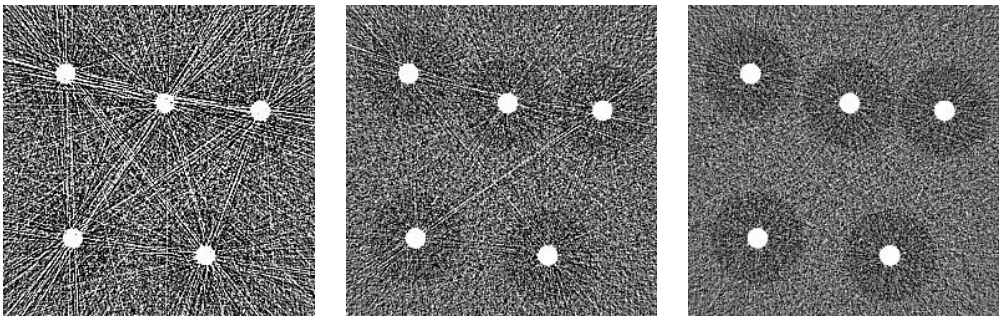

(a) (b) (c)

Figure 8: Extracts of simulated tomographic slices reconstructed from sinograms (400 projections) with Poisson noise in projections. (a) 7.5×10^6 photons per pixel without sample, (b) 1.5×10^7 photons, and (c) 3×10^7 photons.

3.6 Polychromatic X-ray beam

The simulations performed in previous sub-sections used a setup with an ideal monochromatic source model. However synchrotrons, like any radiation source, generate a polychromatic spectrum. It is usually monochromatised either by a perfect crystal or by a multilayer based monochromator in order to obtain a monochromatic beam at a given energy [55] (energy resolution of 1.5% typically). But this spectrum can still be corrupted by harmonic components, up to a few percent at the very worst (typically 10^{-4} harmonics rejection), which generates two kinds of artefacts:

1. bright and dark streaks between attenuating structures (similar to those visible in Figure 3);
2. overestimation in the recovered attenuation coefficient in thick regions, with maximal error close to its border; this results in a bowl-shape radial profile in homogeneous areas, which is also called "cupping effect".

Low energy photons are normally preferentially absorbed due to the logarithmic decrease of the attenuation coefficient when the incident energy increases. In other words, photons corresponding to the fundamental component are more likely to be absorbed behind high density structures, this is beam-hardening. Consequently, the mean spectrum energy crossing a given voxel location depends on the incident orientation. The reconstructed slice no longer corresponds to a map of linear attenuation coefficients at the fundamental energy.

We first performed two beam-hardening simulations using a 33 keV X-ray with a Gaussian distribution, with respectively 500 eV and 5 keV FWHM. Figure 9(a) shows that a 500eV FWHM cannot reproduce the streaks visible in Figures 1 and 3. When a FWHM ten times greater is used, those streaks appear slightly (Figure 9(b)).

A new simulation setup was designed to evaluate the degradation due to a slightly polychromatic beam for the composite material. The incident energy spectrum was heuristically split into three components and should be considered as an upper bound for the actual situation:

1. the fundamental component, 33 keV in energy, 97% of the incident beam,
2. the 1^{st} harmonic component, 66 keV in energy, 2% of the incident beam,
3. the 2^{nd} harmonic component, 99 keV in energy, 1% of the incident beam.

Figures 10(a) and 11(a) present slices reconstructed from simulations performed with a monochromatic 33 keV beam to serve as reference with a tungsten and carbon core respectively. Reconstructed slices with harmonics present in the incident beam are shown in Figures 10(b) and 11(b). Artefacts present in Figure 10 are close to the ones observed in Figure 1. Harmonics could thus

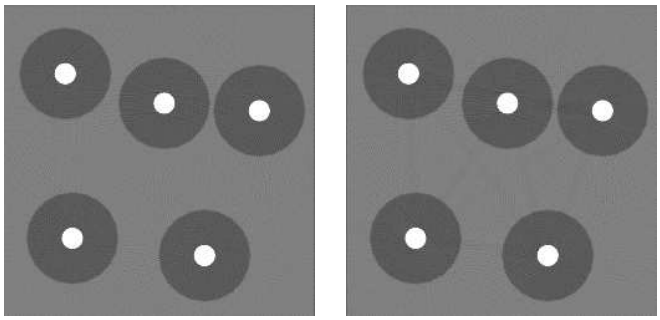

(a) (b)

Figure 9: Extracts of simulated tomographic slices of W-core fibres (acquisition parameter similar to Figure 1). A 33keV X-ray with a Gaussian distibution: (a) 500 eV FWHM, (b) 5keV FWHM.

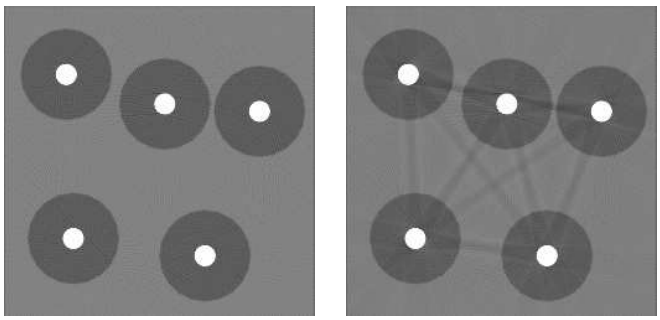

(a) (b)

Figure 10: Extracts of simulated tomographic slices of W-core fibres (acquisition parameter similar to Figure 1). (a) monochromatic case, (b) with harmonics (2% second harmonic, 1% third harmonic).

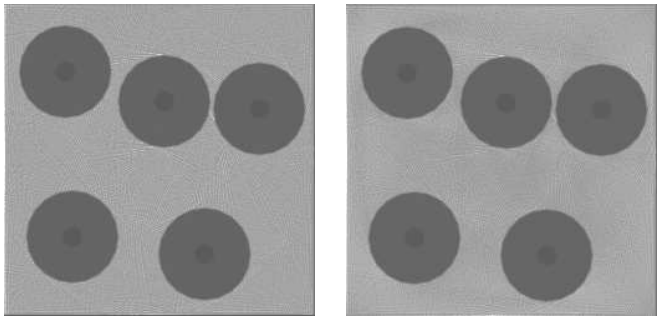

(a) (b)

Figure 11: Extracts of simulated tomographic slices of C-core fibres (acquisition parameter similar to Figure 1). (a) monochromatic case, (b) with harmonics (2% second harmonic, 1% third harmonic).

be one artefact source in this case. It is however possible to deal with polychromatic beams by various means:

- preprocessing the data by calibration procedures [10, 19],
- postprocessing by restoration techniques [18],
- applying a dual energy technique [15].

3.7 Impulse response

Until now, simulations were only performed considering a perfect detector impulse response. Unfortunately, this is not realistic. Indeed, real detectors generally induce blur (also called unsharpness). In X-ray imaging, there could be two main causes of unsharpness: the geometrical unsharpness which is due to the X-ray source extent and the inherent unsharpness which corresponds to the detector impulse response [35]. Both unsharpnesses can be modelled as low-pass and energy dependent convolution kernels. Therefore, without loss of generalisation, since both unsharpnesses convey the same degradations, the artefact study is here restricted to the detector impulse response only. Artefacts caused by such a low-pass filtering of the projections can be quite complex after reconstruction. Their shape in the volume are specific to the material data (non-linear effects). Although there is a global "smoothing" of the reconstructed information, streaks might also appear.

We will investigate the role of the detector in the case of the composite material. The detector inherent unsharpness, also called point spread function (PSF), must first be estimated, but its assessment is not trivial. This depends on various parameters, *e.g.* pixel size, fluorescent screen material, scattering in the fluorescent screen and its support, optical lenses, incident energy, *etc.* The most common methods in use to assess the modulation transfer function (MTF) of linear X-ray detectors, the Fourier transform of the PSF, can be found in a survey by Kaftandjian et al. [30].

Regarding practical considerations, an edge technique was implemented in order to experimentally estimate the edge spread function (ESF) at 33 keV of the beamline camera. It consisted of recovering the unsharpness function via an edge signal derivation, sampled along the intensity gradient of a test object, generally a metal plate [35]. Then, this ESF is derived to obtain the line spread function (LSF), which in turn can be used to estimate the impulse response if circular symmetry is assumed. The pixel size being very small (1.9 µm), the edge material had to be chosen carefully taking into account the possibility to get an edge accurately straight and at the same time to limit fluorescence and scattered photons behind the plate. A gallium arsenide (GaAs) monocrystal plate was used. The edge of the plate is perfectly straight. On the other hand its thickness was 0.5 mm, which was quite large compared to pixel size. Nevertheless, the plate could be positioned perpendicularly to the X-ray beam using a laser-guided calibration. Using a Monte Carlo simulation matching the experimental setup, it was ascertained that scattering and fluorescence did not degrade the experimental measurements: more than 99.9% of the energy received by the detector behind the plate came from directly transmitted photons.

The easiest way to obtain the ESF from a projection is to extract a profile perpendicular to the edge of the test object. But this method lacks accuracy because when there are only few pixels along the intensity drop (Figure 12), the uncertainty is too high to approximate the shape of the profile by an analytic model or to be derived numerically. Two methods can be implemented to handle this lack of data points:

1. The edge can be moved along the intensity gradient direction [35, 30]. A pixel being hidden behind the object becomes 'visible'. Ideally, the motion span is at least equal to the unsharpness support. The step magnitude should be computed to get the required number of projections.

2. The test object has a long sharp edge, slightly twisted relative to a line (or column) of the camera. Therefore an oriented edge profile can be extracted with enough data points in the intensity fall [35, 26].

If the edge object can be accurately moved, the first method is easy to carry out. Figure 12 shows the experimental ESF profile estimated using a translation vector of 0.1 µm, then fitted by the following analytic model (using a nonlinear least-squares algorithm [2])

$$\mathrm{ESF}(x) = a + b \times \left(\arctan\left(\frac{x-c}{d}\right) + \mathrm{erf}\left(\frac{x-c}{e}\right)\right) \tag{2}$$

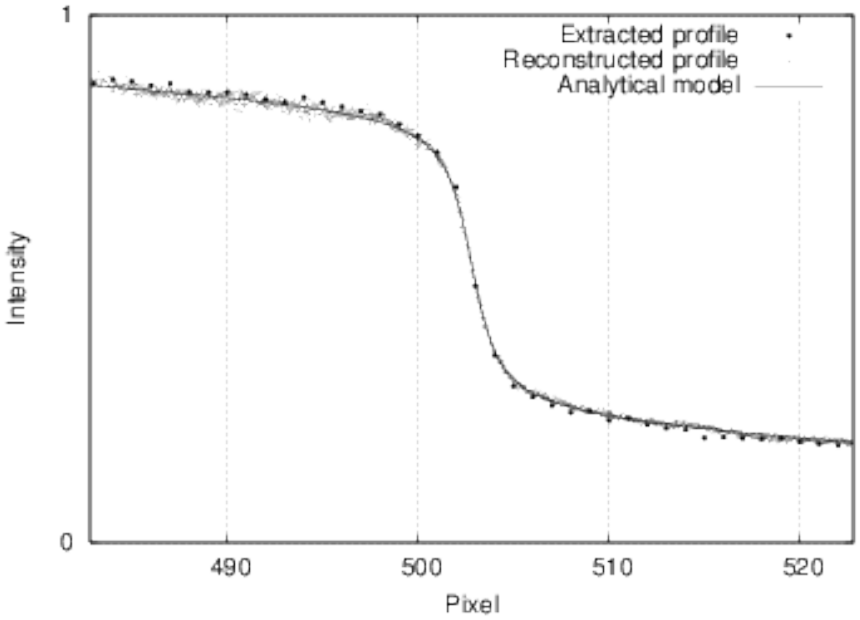

Figure 12: Profile of a GaAs crystal plate using a 0.1 µm translation step (small dots) reconstructed by an analytical model (line). The bigger dots correspond to a single line profile normal to the edge extracted from one projection.

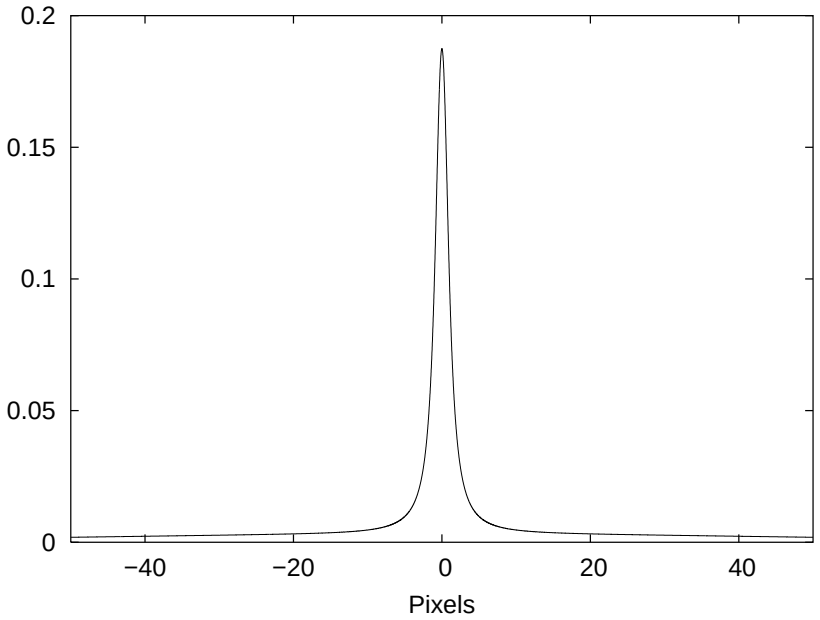

Figure 13: Estimated LSF of the beamline detector.

We can see that the reconstructed profile, given by the translating edge technique, has far more points in the intensity drop than a simple static profile extracted from a single projection. Finally, the analytic expression of the ESF was derived to obtain an estimation of the LSF of the detector, given in Figure 13 (see [26]). To simulate the artefacts caused by this impulse response, the sinograms used to get the reference simulated slices are convolved using the estimation of this impulse response as convolution kernel. Slices in Figure 14, and profiles in Figure 15 show the result

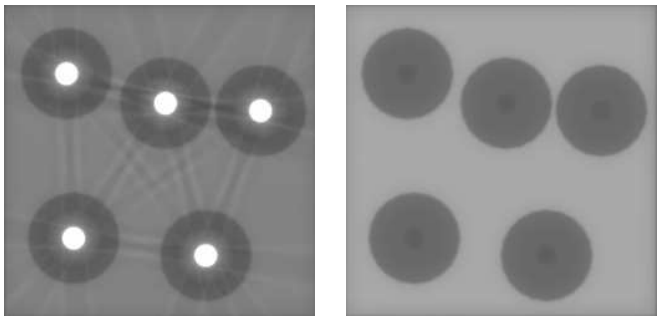

(a) (b)

Figure 14: Simulated tomographic slices with a real detector response (Figure 13) and a monochromatic incident beam (33 keV in energy). (a) fibres with tungsten cores, (b) fibres with carbon cores.

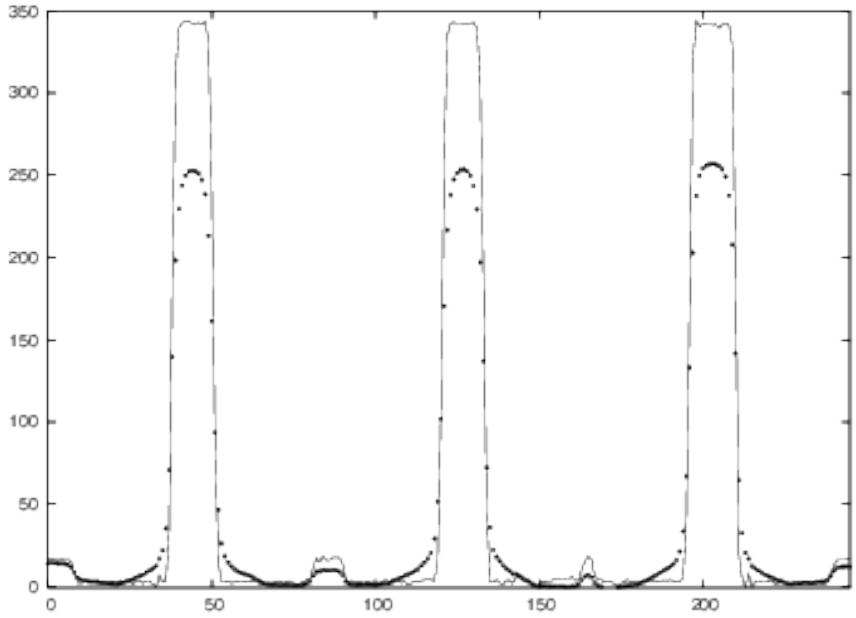

Figure 15: Comparison between an intensity profile extracted from a simulated tomographic slices with an ideal (solid line) and real (dots) detector response. The profile crosses the top three fibre cores. The corresponding slices are given in figures 14(a) and 10(a)

of such simulations. Compared to the ideal detector case, shown in Figure 10(a) and Figure 11(a), there are no visual changes in the case of carbon cores except for a global smoothing, whereas for tungsten cores, the detector impulse response generates dark streaks bordered with bright lines and considerably reduced attenuation coefficients in the core areas: the linear attenuation coefficient of the tungsten drops to $\mu = 250\,\mathrm{cm}^{-1}$ with $\sigma = 7.5\,\mathrm{cm}^{-1}$. Those streaks are quite similar to the artefacts caused by harmonics.

The artefacts due to the impulse response of the detector, and more globally, due to the different sources of unsharpness or non-linearity, can be handled by deconvolution or iterative deblurring techniques [53, 2], but they have to be implemented with caution as they may increase the noise level.

3.8 Defective or badly corrected pixels

The pixels of a CCD detector inherently differ in sensitivity. To deal with this non-uniformity of sensitivity, a flat-field correction (subtraction of a dark image and normalisation by an image acquired in the same conditions but without sample) is applied on every projection of a sinogram before reconstruction by tomography. Nevertheless, flat-field correction might be unable to cancel the effect, which typically creates ring artefacts (Figure 16). This is made worse by the noise accentuating effect of the pre-filtering step of reconstruction algorithms. There are several ways to reduce this kind of artefact, using mechanical devices[17] or filtering techniques [42]. Note that local (temporally and spatially) recurring fluctuations of the beam intensity, which might occur during data acquisition in some synchrotron beamline setups, translate to rings that cannot be easily reduced.

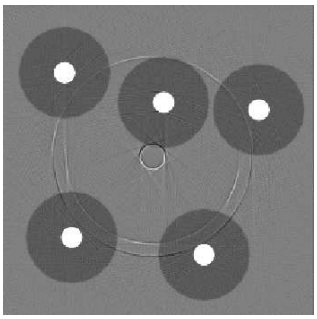

Figure 16: Extract of a simulated tomographic slice using few slightly defective pixels (intensity modified by + or - 5%) in the "light field" image during flat-field correction.

3.9 Phase Contrast

The usual way to produce an image using X-rays is by beam attenuation. However, the contrast present in an X-ray image can also be produced by the optical phase of the transmitted wave [16, 45, 3]. Phase contrast is related to Fresnel diffraction, near-field interference pattern from optics based on wave propagation in the visible light [9]. Phase contrast typically generates fringes at the edges of objects in images reconstructed by tomography. Although this phenomenon is advantageously used in phase contrast tomography [13] and holotomography [12], it could become a source of artefacts in common quantitative microtomography. They appear as black and white overshoots in the volume, similar to the output resulting from an image enhancement technique like unsharp masking [29] with a Laplacian filter. It has indeed been shown that phase contrast contribution at short distances can be related to the Laplacian of the phase image [14].

To simulate phase contrast for the composite material, a program developed at ESRF was used [11]. Both cases with carbon and tungsten cores were simulated for a distance of 80 mm between the sample and the detector. Corresponding projections are shown in Figures 17(a) and 17(b). Figures 18(a) and Figure 18(e) correspond to reference slices, with an ideal detector response and without simulating the phase contrast.

On the other hand, Figure 18(b) and Figure 18(f) present the result of simulations, still using a perfect detector response, taking into account phase contrast. The phase contrast clearly generated artefacts corresponding, on these slices, to dark and bright fringes located along density edges in the volume. To check the effect of phase contrast combined with an estimation of the impulse response of the detector, previous simulated sinograms were convolved by the LSF in Figure 13. Considering a real detector (Figure 18(c) and Figure 18(g)), phase contrast artefacts do not change much for the composite with carbon core fibres, whereas it considerably reduces artefacts around the tungsten core. The corresponding radial profiles of the tungsten core fibre are plotted in Figure 19. These latest simulations seem to be in adequacy with reality, *i.e.* Figure 18(h) (line-point plot of Figure 19) is closer to Figure 18(g) (solid plot of Figure 19) than to Figure 18(f)

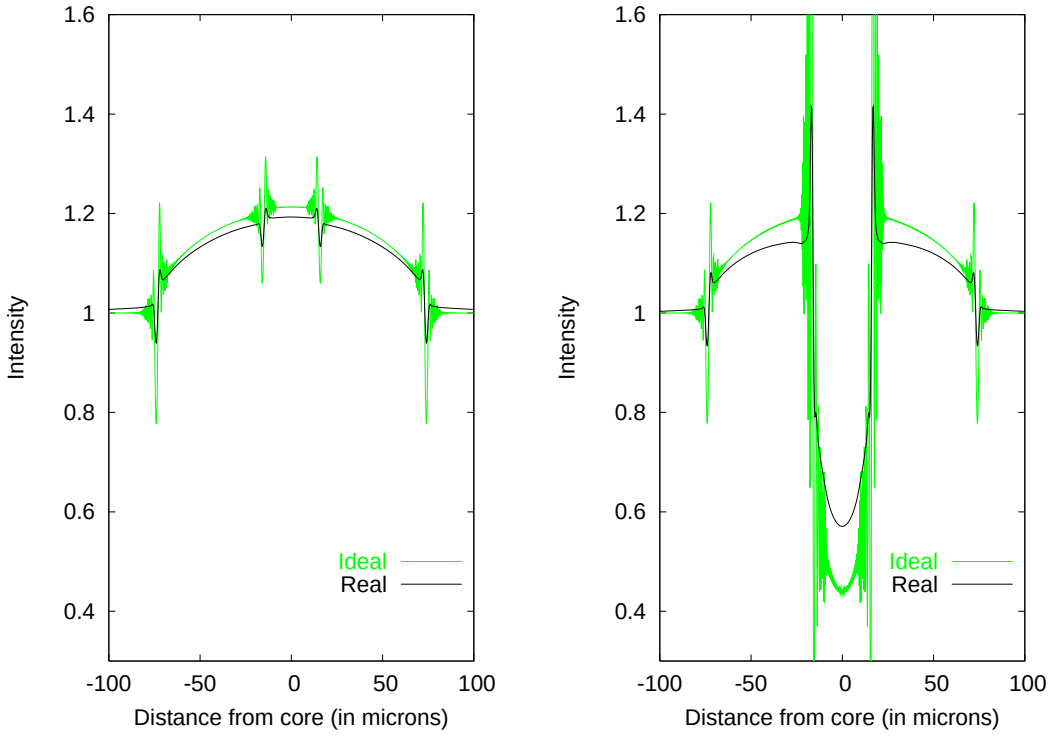

Figure 17: Simulated radiographic intensity profiles of (a) a C-core fibre and (b) a W-core fibre. The grey lines stand for the theoretical incident X-ray intensities, while the black lines represent the X-ray intensities degraded by the detector's MTF.

(dashed plot of Figure 19), which suggests that the detector impulse response does cause the streak artefacts present in Figure 1.

If it is desirable to reduce phase artefacts, the easiest way is to reduce the detector-to-object distance. This is not always possible, for example due to the sample environment. Note that these phase patterns can also be advantageously used as an alternative way to estimate the detector PSF [32].

4 Discussion

We have presented an approach to evaluate many possible causes of artefacts, using both experimental data and simulation tools, in X-ray microtomography by synchrotron radiation. For illustration and coherence purposes, it has been applied throughout the paper to the case of a composite reinforced with alignments of fibres with tungsten cores.

This study showed that when such highly attenuating structures are present in a sample, a few percent harmonics in the incident synchrotron beam is sufficient to produce strong streak artefacts. Artefacts translated by the energy resolution (FWHM) of the monochromatised X-ray distribution remain negligible. We must however note that, with synchrotron radiation, the polychromatic beam is typically monochromatised using a multilayer, which rejects harmonics far below percent level. Nevertheless, care must be taken before rejecting the polychromatism as a probable cause of artefacts in synchrotron microtomography.

This study also highlighted the critical role of the detector impulse response in the production of artefacts. They are similar to those produced by beam hardening. Although the experimental LSF of the beamline detector is quite peaked and narrow, the long tails extending to its sides

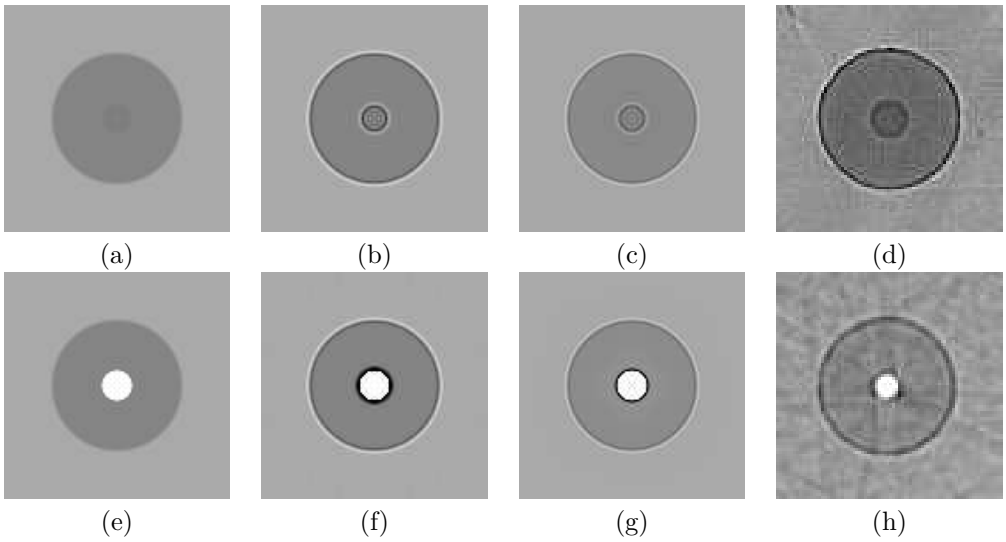

Figure 18: Simulated tomographic scans. Incident beam, 33 keV in energy. Distance between detector and sample, 80 mm. Pixel size 1.9 µm. 900 projections, angular span 180°. Matrix in Ti-6Al-4V, Fibre in silicon carbide. (a), (b), (c) & (d) carbon core. (e), (f), (g) & (h) tungsten core. (a) & (e) with an ideal detector and without phase contrast. (b) & (f) with an ideal detector and with phase contrast. (c) & (g) with a detector (using an estimated impulse response) and with phase contrast. (d) & (h) Extract of tomographic slices from Figure 4 and Figure 1.

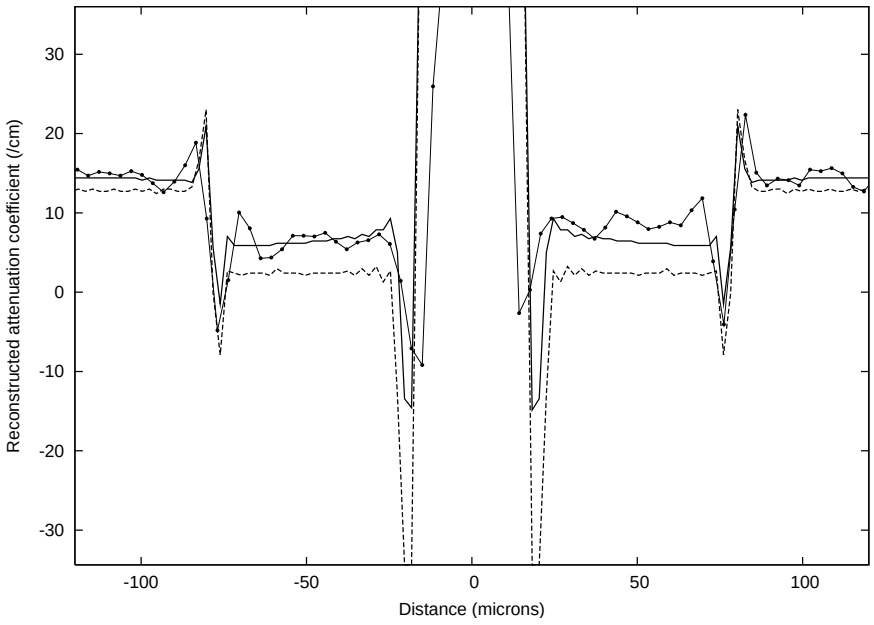

Figure 19: Plot of the radial profiles through Figure 18(f) with a dashed line, Figure 18(g) with a solid line and Figure 18(h) with a thin line-point.

considerably reduce the image contrast of the input projections. This results in a similar degradation to a non-linear detector response. These tails are probably due to residual fluorescence of the 0.5 mm thick substrate supporting the YAG:Ce fluorescent layer deposited. They could also be due to total internal reflections in the fluorescent screen.

The investigation approach developed in this study takes advantage of probabilistic and de-

terministic virtual imaging techniques. This can be applied to any tomographic acquisitions to provide a better understanding and evaluation of artefacts with regard to the corresponding experimental parameters, and to eventually reduce them. This study clearly shows that artefacts present in specific microtomographic volumes acquired by synchrotron radiation can be accurately discriminated and identified using computerised simulations. These results justify a larger study, currently underway, to address the feasibility of incorporating a software solution based on virtual X-ray imaging to remove some specific artefacts automatically, namely those due to secondary radiations and the detector impulse response.

Acknowledgements

We would like to thank P. Duvauchelle and N. Freud for their expertise in virtual X-ray imaging, C. Gonzalez for providing the materials, É. Maire and J.-Y. Buffière for performing the tomographic acquisition of the Ti/SiC fibre composites at ESRF.

References

[1] S. Agostinelli, J. Allison, K. Amako, J. Apostolakis, H. Araujo, P. Arce, M. Asai, D. Axen, S. Banerjee, G. Barrand, and *et al.* Geant4 – a simulation toolkit. *Nuclear Instruments and Methods in Physics Research Section A: Accelerators, Spectrometers, Detectors and Associated Equipment*, 506(3):250–303, July 2003.

[2] R. Aster, B. Borchers, and C. H. Thurber. *Parameter Estimation and Inverse Problems.* Academic Press, 2004.

[3] A. Authier. *Dynamical theory of X-ray diffraction*, volume 11 of *IUCr Monographs on Crystallography.* Oxford Science Publications, 2004.

[4] M. J. Berger and J. H. Hubbell. XCOM: Photons cross sections on a personal computer. Technical Report 87-3597, NBSIR, 1987.

[5] M. J. Berger, J. H. Hubbell, S. M. Seltzer, J. S. Coursey, and D. S. Zucker. XCOM : Photon cross section database. Online (2004, June 21), NIST, 1999. <`http://physics.nist.gov/-PhysRefData/-Xcom/-Text/-XCOM.html`>.

[6] A. Bonin, B. Chalmond, and B. Lavayssière. Monte-carlo simulation of industrial radiography images and experimental designs. *NDT&E International*, pages 503–510, 2002.

[7] S. Bonnet, A. Koenig, S. Roux, P. Hugonnard, R. Guillemaud, and P. Grangeat. Dynamic X-ray computed tomography. *Proceedings of the IEEE*, 91(10):1574–1587, 2003.

[8] S. Bonnet, F. Peyrin, F. Turjman, and R. Prost. Multiresolution reconstruction in fan-beam tomography. *IEEE Trans. on Image Processing*, 11(3):169–176, 2002.

[9] M. Born and E. Wolf. *Principles of optics; electromagnetic theory of propagation, interference, and diffraction of light.* Cambridge University Press, 7th ed. edition, 1999.

[10] R. A. Brooks and G. D. Chiro. Beam hardening in X-ray reconstructive tomography. *Phys. Med. Biol.*, 21(3):390–398, 1976.

[11] P. Cloetens. *Contribution to Phase Contrast Imaging, Reconstruction and Tomography with Hard Synchrotron Radiation.* PhD thesis, Vrije Universiteit Brussel, 1999.

[12] P. Cloetens, W. Ludwig, J. Baruchel, D. Van Dyck, J. Van Landuyt, J. P. Guigay, and M. Schlenker. Holotomography: Quantitative phase tomography with micrometer resolution using hard synchrotron radiation x rays. *Appl. Phys. Lett.*, 75:2912–2914, 1999.

[13] P. Cloetens, W. Ludwig, H. Helfen, S. Salvo, R. Mache, and M. Schlenker. Quantitative phase contrast tomography using coherent synchrotron radiation. In *Proceedings of SPIE Vol. 4503, Developments in X-Ray Tomography III*, pages 82–91, Aug. 2001.

[14] P. Cloetens, M. Pateyron-Salomé, J. Y. Buffière, G. Peix, J. Baruchel, F. Peyrin, and M. Schlenker. Observation of microstructure and damage in materials by phase sensitive radiography and tomography. *J. Appl. Phys.*, 81:5878–5886, 1997.

[15] A. J. Coleman and M. Sinclair. A beam-hardening correction using dual-energy computed tomography. *Phys. Med. Biol.*, 30(11):1251–1256, 1985.

[16] J. Cowley. *Diffraction Physics*. North-Holland Amsterdam, 1975.

[17] G. Davis and J. Elliott. X-ray microtomography scanner using time-delay integration for elimination of ring artifacts in the reconstructed image. *Nuclear Instruments and Methods in Physics Research Section A: Accelerators, Spectrometers, Detectors and Associated Equipment*, 394:157–162, 1997.

[18] J.-M. Dinten and J. Volle. Physical model based restoration of mammographies. In *SPIE Conference on Physics of Medical Imaging, San Diego, California*, pages 641–650, 1998.

[19] N. Douarche, D. Rouby, G. Peix, and J. Jouin. Relations between X-ray tomography, density and mechanical properties in carbon-carbon composites. *Carbon*, 39(10):1455–1465, 2001.

[20] P. Duvauchelle, N. Freud, V. Kaftandjian, and D. Babot. A computer code to simulate x-ray imaging techniques. *Nuclear Instruments and Methods in Physics Research B*, pages 245–258, 2000.

[21] P. Duvauchelle, N. Freud, V. Kaftandjian, G. Peix, and D. Babot. *X-Ray Tomography in Material Science*, chapter 9. Simulation tool for X-ray imaging techniques, pages 127–136. HERMES Science Publications, 2000.

[22] J. Foley, A. van Dam, S. Feiner, and J. Hughes. *Computer graphics: principles and practice*. Addison-Wesley, 2nd EDITION in C, 1997.

[23] N. Freud, P. Duvauchelle, and D. Babot. Simulation of x-ray NDT imaging techniques. In *15th World Conference on Non-Destructive Testing, Roma, 15-21 October 2000*. Italian Society for Non-Destructive Testing and Monitoring Diagnostics (AIPnD), 2000.

[24] G. W. Goerres, C. Burger, E. Kamel, B. Seifert, A. H. Kaim, A. Buck, T. C. Buehler, and G. K. von Schulthess. Respiration-induced Attenuation Artifact at PET/CT: Technical Considerations. *Radiology*, 226(3):906–910, 2003.

[25] M. Grass, R. Koppe, E. Klotz, R. Proksa, M. H. Kuhn, H. Aerts, J. Op de Beek, and R. Kemkers. Three-dimensional reconstruction of high contrast objects using C-arm image intensifier projection data. *Computerized medical imaging and graphics*, 23(6):311–321, 1999.

[26] P. B. Greer and T. van Doorn. Evaluation of an algorithm for the assessment of the MTF using an edge method. *Medical Physics*, pages 2048–2059, 2000.

[27] G. N. Hounsfield. Computerized transverse axial scanning (tomography): Part 1. description of system. *Br J Radiol*, pages 1016–1022, 1973.

[28] J. Hsieh, C. L. Slack, S. Dutta, C. L. Gordon, J. Li, and E. Chao. Adaptive view synthesis for aliasing artifact reduction. In *SPIE-Int. Soc. Opt. Eng. Proceedings of Spie - the International Society for Optical Engineering*, volume 4320, pages 673–80, 2001.

[29] A. K. Jain. *Fundamentals of digital image processing*. Prentice-Hall, Inc., 1989.

[30] V. Kaftandjian, Y. M. Zhu, G. Rozière, G. Peix, and D. Babot. A comparison of the ball, wire, edge, and bar/space pattern techniques for modulation transfer function measurements of linear x-ray detectors. *Journal of X-Ray science and technology*, pages 205–221, 1996.

[31] A. Kak and M. Slaney. *Principles of Computerized Tomographic Imaging*. IEEE PRESS, 1988.

[32] A. Koch, C. Raven, P. Spanne, and A. Snigirev. X-ray imaging with subminrometer resolution employing transparent luminescent screens. *Journal of the Optical Society of America A*, 15(7):1940–1951, 1998.

[33] R. Koppe, E. Klotz, M. Grass, V. Rasche, J. Op de Beek, and J. Moret. Die 3-D-rotationsangiographie (3-D-RA) in der neuroradiologie. *Klinische Neuroradiologie*, 13(2):55–65, 2003.

[34] J. C. Labiche, J. Segura-Puchades, D. Van Brussel, and J. P. Moy. Frelon camera: fast readout low noise. *ESRF Newsletter*, 25:41–43, 1996.

[35] J.-M. Létang and G. Peix. On-line x-ray focal spot assessment based on deconvolution using standart imaging devices. *NDT&E International*, pages 303–317, 2003.

[36] J.-M. Létang, N. Freud, and G. Peix. Signal-to-noise ratio criterion for the optimization of dual-energy acquisition using virtual x-ray imaging: application to glass wool. *Journal of Electronic Imaging*, 13(3):436–449, 2004.

[37] E. Maire and J.-Y. Buffière. X-ray tomography of aluminium foams and Ti/SiC composites. In *X-Ray Tomography in Material Science*, pages 121–125. HERMES Science Publications, 2000.

[38] G. Michael. X-ray computed tomography. *Physics Education*, 36(6):442–451, 2001.

[39] B. Ohnesorge, T. Flohr, K. Schwarz, J. P. Heiken, and K. T. Bae. Efficient correction for ct image artifacts caused by objects extending outside the scan field of view. *Medical Physics*, 27(1):39–46, Jan. 2000.

[40] G. Penney, P. Batchelor, D. Hill, and D. H. J. Weese. Validation of a two- to three-dimensional registration algorithm for aligning preoperative CT images and intraoperative fluoroscopy images. *Medical Physics*, 28(6):1024–1032, 2001.

[41] G. Ramachandran and A. Lakshminarayanan. Three dimensional reconstruction from radiographs end electron micrographs: Application of convolution instead of fourier transforms. *Proc. Nat. Acad. Sci.*, 68:2236–2240, 1971.

[42] C. Raven. Numerical removal of ring artifacts in microtomography. *Review of Scientific Instruments*, 69(8):2978–2980, 1998.

[43] J. E. Roos, J. K. Willmann, D. Weishaupt, M. Lachat, B. Marincek, and P. R. Hilfiker. Thoracic Aorta: Motion Artifact Reduction with Retrospective and Prospective Electrocardiography-assisted Multi-Detector Row CT. *Radiology*, 222(1):271–277, 2002.

[44] F. Salvat, J. M. Fernández-Varea, and J. Sempau. *PENELOPE - A Code System for Monte Carlo Simulation of Electron and Photon Transport*. Nuclear Energy Agency, OECD, 2003. Workshop Proceedinds, Issy-les-Moulineux, France, 7-10 July 2003, 253p.

[45] E. J. Samuelsen, P.-J. Houen, O. W. Gregersen, T. Helle, and C. Raven. Three-dimensional imaging of paper by use of synchrotron x-ray microtomography. In *International Paper Physics Conference*, pages 307–312, 1999.

[46] X. Tang, R. Ning, R. Yu, and D. Conover. Cone beam volume ct image artifacts caused by defective cells in x-ray flat panel imagers and the artifact removal using a wavelet-analysis-based algorithm. *Medical Physics*, 28(5):812–825, May 2001.

[47] P. S. Tofts and J. C. Gore. Some sources of artefact in computed tomography. *Phys. Med. Biol.*, 25(1):117–127, 1980.

[48] A. Watt. *3D Computer Graphics*, chapter Rays and computer graphics, pages 17–25. Addison-Wesley, 3rd edition, 2000.

[49] J. Weese, R. Gocke, G. Penney, P. Desmedt, T. Buzug, and H. Schumann. Fast voxel-based 2D/3D registration algorithm using a volume rendering method based on the shear-warp factorization. In *Medical Imaging: Image Processing*, pages 802–810. SPIE, 1999.

[50] M. Wevers, P. De Meester, and R. Swennen. Microfocus x-ray computer tomography in materials research. In *15th World Conference on Non-Destructive Testing, Roma, 15-21 October 2000*. Italian Society for Non-Destructive Testing and Monitoring Diagnostics (AIPnD), 2000.

[51] B. R. Whiting, E. C. Mcfarland, and J. A. Brink. Influence of image acquisition parameters on ct artifacts and polyp depiction in spiral ct colonography: in vitro evaluation. *Radiology*, 217(1):165–172, Oct. 2000.

[52] J. Wiegert, M. Bertram, J. Wulff, D. Schäfer, J. Weese, T. Netsch, H. Schomberg, and G. Rose. 3D ROI for cone-beam computed tomography. *International Congress Series*, 1268:7–12, 2004.

[53] J. F. Williamson, B. R. Whiting, J. Benac, R. J. Murphy, G. J. Blaine, J. A. O'Sullivan, D. G. Polittle, and D. L. Snyder. Prospects for quantitative computed tomography imaging in the presence of foreign metal bodies using statistical image reconstruction. *Medical Physics*, 29(10):2404–2418, 2002.

[54] C.-K. Yang, S. C. Orphanoudakis, and J. W. Strohbehn. A simulation study of motion artefacts in computed tomography. *Phys. Med. Biol.*, 27(1):51–61, 1982.

[55] E. Ziegler, O. Hignette, C. Morawe, and R. Tucoulou. High-efficiency tunable X-ray focusing optics using mirrors and laterally-graded multilayers. *Nuclear Instruments and Methods in Physics Research A*, 467-468:954–957, 2001.